Hot carriers in mixed Pb-Sn halide perovskite semiconductors cool slowly while retaining their electrical mobility

Maurizio Monti,[1,*] K. D. G. Imalka Jayawardena,[2] Edward Butler-Caddle,[1] Rajapakshe M. I. Bandara,[2] Jack M. Woolley,[3] Michael Staniforth,[1,3] S. Ravi P. Silva,[2] and James Lloyd-Hughes[1,†]

[1]*Department of Physics, University of Warwick, Gibbet Hill Road, Coventry, CV4 7AL, United Kingdom*

[2]*Advanced Technology Institute, Department of Electrical and Electronic Engineering, University of Surrey, Guildford, Surrey, GU2 7XH, United Kingdom*

[3]*Department of Chemistry, University of Warwick, Gibbet Hill Road, Coventry, CV4 7AL, United Kingdom*

(Received 14 September 2020; revised 25 November 2020; accepted 30 November 2020; published 24 December 2020)

The electron-phonon interaction controls the intrinsic mobility of charges in metal halide perovskites, and determines the rate at which carriers lose energy. Here, the carrier mobility and cooling dynamics were directly examined using a combination of ultrafast transient absorption spectroscopy and optical pump, THz probe spectroscopy, in perovskites with different lead and tin content, and for a range of carrier densities. Significantly, the carrier mobility in the "hot phonon bottleneck" regime, where the LO phonon bath keeps carriers warm, was found to be similar to the mobility of cold carriers. A model was developed that provides a quantitative description of the experimental carrier cooling dynamics, including electron-phonon coupling, phonon-phonon coupling and the Auger mechanism. In the Pb and Sn alloy the duration of the hot carrier regime was extended as a result of the slower decay of optical phonons. The findings offer an intuitive link between macroscopic properties and the underlying microscopic energy transfer processes, and suggest new routes to control the carrier cooling process in metal halide perovskites to optimize optoelectronic devices.

DOI: 10.1103/PhysRevB.102.245204

I. INTRODUCTION

In recent years the rapid development of metal halide perovskites has established their potential in photovoltaic devices due to their compelling power efficiencies [1–4]. Significant attention has been paid to the underlying photophysics and photochemistry of halide perovskites, in particular the fundamentals of light absorption and emission, and electrical transport [1,2,5,6]. Photons with energies that substantially exceed the band gap of the light absorber create "hot" carriers whose excess energy is often dissipated as heat, leading to losses in solar cells. It is therefore of fundamental and applied interest to study this energy loss mechanism in candidate materials for photovoltaics. Moreover, the extraction of carriers while hot may provide a route to increase the power efficiency above the Shockley-Queisser limit at room temperature (around 34%) [7].

Interestingly, in halide perovskite semiconductors the so-called "hot phonon bottleneck" (HPB) appears: in certain conditions of high injected carrier densities ($\sim 10^{18}$–10^{19} cm^{-3}) and high photon energies (well above the band gap), hot carriers persist for surprisingly long times [8], permitting transport of hot carriers over significant distances [9] and at densities lower than found in prototypical semiconductors such as GaAs [8]. This has driven a strong interest in understanding the dynamics of hot carriers in halide perovskites [7,8,10,11]. Hot carrier relaxation has been extensively studied in $MAPbI_3$ [8,10] and other lead-based perovskites [7], and also in $FASnI_3$ [12], which showed intriguingly slow relaxation. Most works focused on the study of a single compound or on a small set of compounds, and hence it is not clear how changing the composition influences hot carrier cooling. There is therefore a necessity for more systematic studies on various compositions to understand which parameter, or set of parameters, control hot carrier cooling (HCC).

Transient absorption spectroscopy (TAS) is used widely to investigate nonequilibrium processes on an ultrafast timescale, and has been applied extensively to the study of halide perovskite semiconductors [13–15], in particular to extract carrier temperatures and study the dynamics of the cooling of hot carriers [8,10,16–19]. Recently, optical pump, terahertz probe (OPTP) spectroscopy has also been applied to study the carrier cooling dynamic in perovskites [20–22]. OPTP spectroscopy is a flexible and powerful technique that has been successfully applied to the study of perovskite semiconductors [6,23], thanks to the possibility of extracting recombination times and mobilities in a noncontact fashion. OPTP can further provide information on the carrier cooling dynamic by studying the dynamical rise in the photoconductivity [24,25]. Both OPTP and TAS have been applied to the study of carrier cooling in perovskites, sometimes with apparently contradictory results: almost all experiments performed with TAS show an extremely long carrier cooling time, exceeding 100 ps [8–10], an effect which is usually absent in OPTP measurements on samples with the same or similar composition [21,22]. This apparent contradiction raises the question of how best to compare the outcomes of these two experimental techniques.

*Current address: Department of Physics and Astronomy, Aarhus University, Ny Munkegade 120, 8000 Aarhus C, Denmark.

†J.Lloyd-Hughes@warwick.ac.uk

The diffusion length L_D of a semiconductor is an important figure of merit and is often used as a predictor of solar cell efficiency. In the diffusive transport regime $L_D = \sqrt{D\tau_R}$ and can exceed a few microns in the halide perovskites, as a result of slow charge carrier recombination times ($\tau_R > 100$ ns) combined with reasonable diffusivities D [6]. The ambipolar diffusion coefficient D can be determined from optical methods that include transient absorption microscopy [9] and PL microscopy [26], which spatially and temporally resolve the carrier density to track the diffusion process. The effective values of D reported vary widely and may even change dynamically, varying depending on the timescale probed by the experiment [9,26]. Since $D = \sqrt{\mu k_B T_c/e}$ for a nondegenerate semiconductor, changes to the mobility μ or to the carrier temperature T_c may account for some of the variation reported in D. Therefore, to better understand the migration of hot carriers in halide perovskites it is particularly desirable to obtain independent measures of μ and T_c under nonequilibrium conditions, including in the HPB regime.

In this work we report a study of hot carrier cooling in mixed metal halide perovskites using a combination of OPTP and TAS, experimentally resolving both μ and T_c independently. We developed a model of hot carrier relaxation that describes the coupling of carriers at temperature T_c to LO phonons at temperature T_p, both above the lattice temperature T_L. By comparing the model and experiment we identify three distinct cooling stages: (1) the Fröhlich regime ($T_c > T_p$), dominated by cooling through electron-LO phonon scattering; (2) the HPB regime ($T_c \sim T_p > T_L$), characterized by a hot LO phonon population that slows the carrier cooling rate, and dominated by the phonon-phonon interaction; (3) the Auger cooling regime ($T_c \sim T_p \gtrsim T_L$), evident at longer delay times for high initial carrier temperatures, and dominated by Auger processes that keep carriers hot. With reference to this model, we elucidate the information accessible by each experimental method, by showing that TAS probes all stages of cooling, while OPTP is sensitive predominantly to stage (1). By determining the mobility and temperature of hot carriers in the HPB stage we demonstrate that hot carriers retain similar mobilities to cold carriers. This justifies the high diffusivities reported in the literature at early times after photoexcitation [9], by directly determining the carrier mobility and temperature for the same samples and experimental conditions. Additionally, a more persistent hot carrier population was found for a Pb-Sn alloy, in comparison to the pure Pb- or Sn-perovskites, and which was linked to slower LO phonon decay.

II. METHODS

A. Sample fabrication

Thin films of the perovskite $Cs_{0.05}(FA_{0.83}MA_{0.17})_{0.95}Pb_xSn_{1-x}I_3$, with $x = 0$, 0.25, 0.5, 0.75, or 1.0, were produced on z-cut quartz substrates by a spin-coating method [27]. As Sn-containing perovskites are known to be more sensitive to degradation in the air [28] samples were prepared in a nitrogen glove box (<1 ppm oxygen) and fully encapsulated to prevent oxygen or moisture exposure during measurement. Films were encapsulated with a second z-cut quartz substrate and sealed by an epoxy. This choice of substrate ensured excellent transparency across the UV, visible, and THz ranges.

B. Ultrafast spectroscopy

The optical-pump, THz-probe spectrometer used has been described previously [20]. Transient absorption spectra were measured using a UV pump, white light probe spectrometer fed by an ultrafast Ti:sapphire amplifier (Newport Spectra Physics Spitfire Ace, 13 mJ, 1kHz, 40 fs). The 400-nm pump was generated from an 800-nm beam using a BBO crystal, while the white light continuum was generated by focusing a 1300-nm beam, generated via an optical parametric amplifier (TOPAS C, Light Conversion), onto a sapphire window. Time resolution was provided by a motorized delay stage. Measurements were performed in transmission by measuring the difference of the unpumped and pumped transmitted intensities (collected by a fiber-coupled spectrometer), to determine the change in optical density upon photoexcitation. The change in optical density is defined by

$$\Delta\text{mOD} = 1000 \log_{10} \frac{I}{I_0}, \tag{1}$$

where I and I_0 are the pumped and unpumped transmitted intensities. Both experiments were performed under nitrogen to limit exposure to oxygen and moisture.

III. RESULTS AND DISCUSSION

Previous work suggested that altering the A-site cation from fully inorganic (Cs) to organic (MA or FA) does not significantly alter the hot carrier cooling times [18,21]. Our work focuses, for the first time, on the study of hot carrier cooling in triple cation mixed lead-tin perovskites $Cs_{0.05}(FA_{0.83}MA_{0.17})_{0.95}\,Pb_xSn_{1-x}(I_{1-y}Br_y)_3$. The choice of a triple-cation on the perovskite A-site was made to improve the sample response thanks to their increased mobility, to enhance their chemical and photostability over time and, finally, to make the findings directly relevant to the current state-of-the-art for perovskite solar cell materials [29], which often contain a small amount of Br. Samples were prepared with $y = 0$ (pure iodine) for different Pb/Sn ratio ($x = 0$, 0.25, 0.5, 0.75, or 1.0, with $x = 1$ corresponding to pure Pb), and also for $x = 1$, $y = 0.17$.

A. Optical characterization

The absorption and photoluminescence (PL) spectra were recorded to assess the sample quality, to provide information on the band-gap energy, and to determine the fraction of photons absorbed at the different pump wavelengths used. The energy gap was determined from Gaussian fits to the PL spectra and from the absorption coefficient [30] for all compositions studied, as reported in Fig. 1(a) for the series with pure iodine ($y = 0$). It is evident that the band gap derived from absorption (red squares) and from PL (blue circles) both show a strong bowing of the gap. The change in band gap with x can be written [31]

$$E_g(x) = xE_{g,1} + (1-x)E_{g,2} - bx(1-x), \tag{2}$$

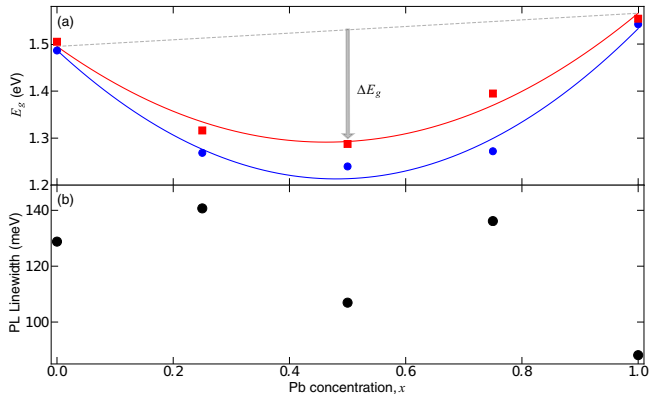

FIG. 1. (a) Band gap versus lead concentration, as determined from absorbance (red squares) and photoluminescence (blue circles). Solid lines are fits following Eq. (2). The dotted line represents the change in band gap in the absence of band bowing, while the arrow indicates ΔE_g. A strong band bowing is evident, with a minimum band gap at $x = 0.5$. (b) FWHM of the PL spectra (black circles) versus Pb concentration.

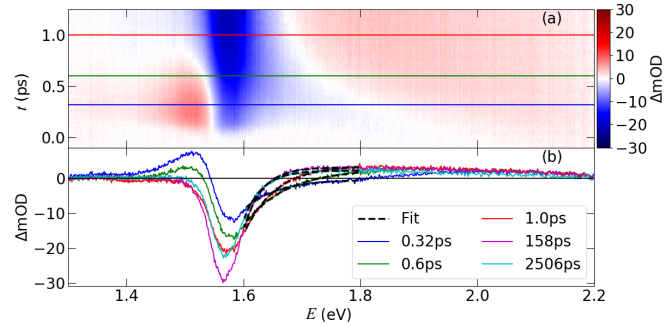

FIG. 2. (a) Transient change in absorption (in mOD) versus probe energy and pump-probe time delay t for $Cs_{0.05}(FA_{0.83}MA_{0.17})_{0.95}PbI_3$. Three prominent features are observed in the spectrum and are discussed in the text: a quick and narrow photoinduced absorption region at the band gap, a strong absorption bleach just above the band gap, and a broad photoinduced absorption at higher energies. The fluence was 70 μJcm^{-2} and the excess energy was 1.8 eV. (b) Transient absorption spectra at different pump-probe delays. Spectra correspond to the time slices in panel (a) are indicated with matching colors. The dashed lines correspond to fits used to extract the carrier temperature.

where $E_{g,i}$ are the band gaps of the pure compounds and b is the bowing parameter. Band bowing is visually represented in Fig. 1(a) as the difference $\Delta E_g = b/4$ between the hypothetical band gap line in the absence of bowing and the actual band gap of the $x = 0.5$ alloy. This expression was fit to the experimental results, from which we obtained $b = 0.95 \pm 0.10$ for the absorbance data and $b = 1.20 \pm 0.12$ for the PL data. The value of b is similar to that found by a study of band bowing in $FAPb_xSn_{1-x}I_3$, which reported $b = 0.73$ eV from absorbance at room temperature [30]. Here the different A-site cations may account for the larger b as the crystal structure, in particular the metal-halide bond lengths and angles, will be subtly different.

The PL linewidth has been suggested to serve as an indicator of whether alloying increases the disorder of the film: local fluctuations in the Pb or Sn concentration may broaden the PL inhomogeneously [30]. Here the linewidth was around 100 meV for all samples [Fig. 1(b)]. Overall, the PL and absorption results demonstrate the successful formation of perovskite alloys with controllable Pb/Sn ratio.

B. Carrier temperature from transient absorption

Ultrafast transient absorption spectroscopy was used to extract the carrier temperature dynamic in samples with different composition. A 400-nm pump pulse excited the perovskite films with 3.1-eV photons, giving excess energies in the range 1.6–1.8 eV (varying slightly with x as a result of the band bowing reported above). We defined the excess energy as $h\nu - E_g$, where $h\nu$ is the pump energy and E_g is the energy gap measured by photoluminescence (PL). We note that due to their similar effective masses [16] we assume that the energy is evenly distributed between electron and holes. A high excess energy was adopted in order to access the HPB regime [32], and a range of pump fluences 40–400 μJcm^{-2} was used. A broadband white light probe provided spectral coverage of the pump-induced absorption change, $\Delta\alpha$, close to the band edge. An example of data obtained for $x = 1$ is reported in Fig. 2(a), where the color represents $\Delta\alpha$ (in mOD) versus probe energy (x-axis) and time (y-axis). Only the first 1.2 ps are reported for clarity. The colored lines represent slices at different pump-probe delays, as reported in Fig. 2(b).

Shortly after $t = 0$, three prominent features appear: a strong negative $\Delta\alpha$ at 1.6 eV, just above the band gap (1.54 eV); a short-lived positive absorption feature at the band gap; and a weak broad photoinduced absorption (PIA) at higher energies. The negative $\Delta\alpha$ is readily identifiable as a ground-state bleach (GSB) from the accumulation of carriers near the band extrema [8,10]. The quick PIA has been alternatively interpreted in different works as arising from excitons [33], band-gap renormalization [10] and polaron formation [34]. The broad PIA region is generally observed [8,10] and was attributed to a photoinduced change of the refractive index [10]. The band-gap PIA quickly disappears within 1 ps, while the broad PIA remains along with the bleach even 2.5 ns after photoexcitation. In Fig. 2(b) spectra at $t = 158$ ps and at $t = 2506$ ps are also presented. The amplitude of the GSB grows slowly to a maximum around 158 ps delay, indicative of slow carrier cooling towards the band edge on this timescale [14,35].

Following an established methodology [8,10,18], the carrier temperature T_c was extracted from the high-energy tail of the GSB at different pump-probe delay times. The function $\Delta\alpha = A_0 e^{-E/k_B T_c} + \Delta\alpha_0$ was used, where A_0 is the equilibrium absorption coefficient and $\Delta\alpha_0$ is an offset added to take into account the influence of the broad PIA at higher energies. Following Ref. [8] the TA spectra were fitted at energies well above the band edge (starting >0.1 eV above the band gap) to allow any influence of electron-hole correlations (excitons), present near the band edge, to be ignored. Although it has been suggested that the cooling dynamics of electron and holes could be different [17], for simplicity we assume that the electron and hole temperatures are equal, on the basis that

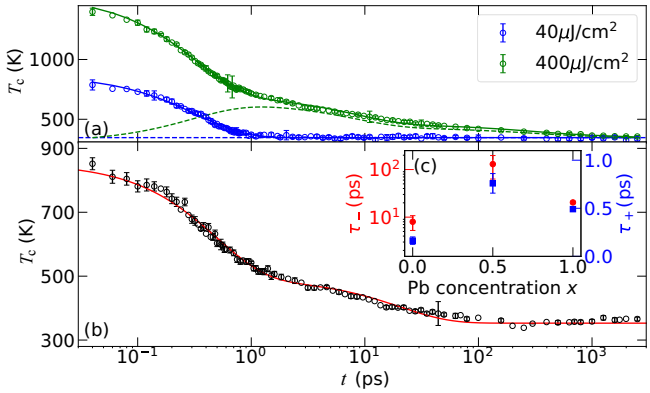

FIG. 3. (a) Carrier temperature T_c versus time for $Cs_{0.05}(FA_{0.83}MA_{0.17})_{0.95}Pb(I_{0.83}Br_{0.17})_3$ at low fluence ($40\mu Jcm^{-2}$, blue circles) and high fluence ($400\mu Jcm^{-2}$, green circles). Continuous lines are fits to T_c using Eq. (3), while dashed lines are the hot phonon temperatures calculated using Eq. (4) and the parameters from the fit to T_c. The elevated temperatures in the 1 to 30 ps range are a product of the hot phonon bottleneck, where $T_c \simeq T_p$, while the slower recovery at later times results from the Auger effect. (b) Cooling dynamic and fit parameters for $Cs_{0.05}(FA_{0.83}MA_{0.17})_{0.95}Pb_xSn_{1-x}I_3$ at 70 μJcm^{-2}. The red line is a fit using the TTM, as detailed in the text, for $x = 1$. The inset (c) reports the fit parameters τ_+ and τ_- for different concentrations x. The short time constant, τ_+ (blue squares, right-hand axis), represents the first cooling stage, while the second, slower cooling stage has time constant τ_- (red circles, left-hand axis).

the excess energy is evenly distributed between electron and holes (as their masses are similar).

In Fig. 3 the extracted carrier temperatures are reported for the composition $x = 1$, $y = 0.17$ at low (40 μJcm^{-2}, blue circles) and high (400 μJcm^{-2}, green circles) fluence. At low fluence the carrier temperature starts at about 800 K but within 1 ps drops to close to room temperature, i.e., only a single, fast decay process is evident. The carriers cool to the lattice temperature, $T_L = 363 \pm 3$ K, which remains above room temperature for the rest of the experimental time window (3 ns) as a result of the low thermal conductivity of halide perovskites [36]. In contrast to the low fluence case, at high fluence an abrupt change to a slower dynamic can be clearly seen from 1 ps onwards. This effect has been observed many times in metal halide perovskites [8,10] and inorganic semiconductors, and can be attributed to the hot phonon bottleneck. A fluence of 70 μJcm^{-2} was found to be sufficient to access the HPB regime for $x = 1$, $y = 0$, and hence this fluence was adopted to examine the influence of Pb content (samples with varying x).

Before returning to the experimental results, we first elucidate the different mechanisms contributing to carrier cooling in more detail, with reference to a model that captures the relevant microscopic physical processes and that links them to macroscopic parameters.

C. Modeling hot carrier cooling dynamics

We developed a phenomenological approach based on the three-temperature model (TTM), which was applied previously to the electron-phonon interaction in the metals Au and Ag [37] and to spin-lattice relaxation in manganite oxides [38]. Our approach is intended to provide an intuitive and quantitative way to describe the different cooling regimes, including the hot phonon bottleneck mechanism, in halide perovskites. Previously, two analysis methods have been reported: an empirical approach, aimed to obtain a quantitative fit to experimental data but without links to the microscopic mechanisms [19], and a more complete microscopic approach [16]. This second approach calculated the energy loss rate including the heating of the phonon population in the Fröhlich scattering model. This is complex to implement, computationally demanding, and requires a detailed knowledge of microscopic quantities such as the effective mass, static, and high frequency dielectric constants, and LO phonon energies. Some of these constants are difficult to measure in particular halide perovskites: for instance Sn-rich compounds exhibit high levels of p-doping, making it difficult to determine phonon frequencies and the static dielectric constant [39]. Further, these parameters are often unknown for more complex compounds, such as the triple cation alloys investigated in this work.

1. TTM: Mathematical description

Here, in the TTM a pair of coupled rate equations describe the interaction of the carrier temperature T_c with the phonon temperature T_p, and the coupling of the phonons to the lattice, at temperature T_L. Note that this approach is sometimes called the *two* temperature model in the literature: we refer to it as the three temperature model to highlight the independent temperatures of the three subsystems. The rate equations proposed are as follows:

$$C_c \frac{dT_c}{dt} = -G_{cp}(T_c - T_p) + G_A(T_g + T_c), \tag{3}$$

$$C_p \frac{dT_p}{dt} = +G_{cp}(T_c - T_p) - G_{pp}(T_p - T_L), \tag{4}$$

where C_c, C_p, G_{cp}, G_{pp} are the carrier heat capacity, the phonon heat capacity, the electron-phonon coupling constant, and the phonon-phonon coupling constant, respectively. The terms $\pm G_{cp}(T_c - T_p)$ correspond to coupling between hot carriers and hot phonons, while the coupling of hot phonons to the lattice is described by $G_{pp}(T_p - T_L)$. The last term in Eq. (3) represents Auger heating, where $T_g = 2E_g/3k_B$ and $G_A = k_A N^2(t)$ for Auger recombination rate k_A and carrier density $N(t)$. These equations are not solvable analytically, so a numerical solution is, in general, necessary. The experimental carrier temperature was fitted using a numerical solution to Eq (3). As reported in Fig. 3(a), an excellent match with the experimental data was obtained, yielding: $G_{cp}/C_c = 2.3$THz, $G_{pp}/C_p = 0.2$THz, and $G_A(0)/C_c = 0.14$THz. The Auger heating term is thought to be important for perovskites [16] and its inclusion was necessary here to model the long-lived tail in T_c evident at high excitation fluences (e.g., at 400 μJcm^{-2} in the figure). The dashed lines in Fig. 3(a) indicate the phonon temperature calculated using the same parameters in Eq. (4), and allow the HPB regime, $T_c = T_p$, to be readily identified.

At lower fluence ($<100\ \mu\mathrm{Jcm}^{-2}$) the Auger term was not needed to correctly reproduce the dynamics. Hence, lower fluences were used to investigate different compositions in this work. This has the benefit of yielding analytical solutions to the rate equations: when the Auger term can be neglected, and subject to the initial conditions $T_c(t=0)=T_0$ and $T_p(t=0)=T_L$, the carrier and hot phonon temperatures are

$$T_c(t) = T_L + A_+(T_0-T_L)e^{-t/\tau_+} + A_-(T_0-T_L)e^{-t/\tau_-}, \quad (5)$$

$$T_p(t) = T_L + B_+(T_0-T_L)e^{-t/\tau_+} + B_-(T_0-T_L)e^{-t/\tau_-}. \quad (6)$$

After the pump pulse has rapidly heated the carriers to T_0, the hot carrier temperature recovers exponentially, with a fast time constant τ_+, and a slower decay given by τ_-. The decay rates $k_\pm = 1/\tau_\pm$ are

$$\frac{1}{\tau_\pm} = \frac{G_{cp}+G_{pp}}{2C_p} + \frac{G_{cp}}{2C_c} \pm \frac{1}{2}\sqrt{\left(\frac{G_{cp}+G_{pp}}{C_p} - \frac{G_{cp}}{C_c}\right)^2 + \frac{4G_{cp}^2}{C_cC_p}}, \quad (7)$$

and the amplitudes of the terms in Eqs. (5) and (6) are $A_+ = (k_0-k_-)/(k_+-k_-)$, $A_- = (k_+-k_0)/(k_+-k_-)$, $B_+ = (\frac{k_-}{k_0}-1)A_-$, $B_- = (\frac{k_+}{k_0}-1)A_+$, with $k_0 = G_{cp}/C_c$. The dimensionless amplitudes $A_\pm$ control the relative weight of the fast and slow components, and obey the expression $A_+ + A_- = 1$.

We note that Eq. (5) corresponds to the sum of two exponential decays, for which the amplitudes and decay rates are the fit parameters if T_L and T_0 are known. The amplitudes and decay rates can be reliably determined from one $T_c(t)$ curve as the decays have quite different rates. An excellent agreement of the fit from Eq. (5) with the experimental T_c dynamic was obtained, as evident for a sample with $x=1, y=0$ in Fig. 3(b), where the fit yielded $\tau_+ = 0.49 \pm 0.02$ ps and $\tau_- = 20 \pm 1.3$ ps, while $A_\pm = 0.72$ and 0.28, respectively. We now provide physical insights into the TTM model and its free parameters, which from Eq. (7) are the rates G_{cp}/C_c, G_{cp}/C_p, and G_{pp}/C_p.

2. TTM: Physical description

The TTM assumes that the carrier temperature is coupled with the phonon temperature via a coupling constant G_{cp}. When the carrier temperature T_c is high, the efficient carrier-LO phonon interaction transfers energy from carriers to the LO-phonon bath, raising its temperature T_p. This process takes around 1 ps [Fig. 3(a)]. The LO-phonon bath tries to reduce its temperature by LO-phonons decaying into lower-energy acoustic and/or optical phonons, at a rate controlled by the coupling constant G_{pp}. In general, the fast and slow decay times $\tau_\pm$ cannot be uniquely identified with carrier-phonon coupling and LO-phonon decay, as both terms enter into Eq. (7). However, we now describe the underlying physical processes in detail to gain insights into their relative magnitude, and show that for certain values of the parameters the fast decay time τ_+ is dominated by carrier-phonon coupling, while τ_- is controlled by the hot phonon decay rate.

In general, the phonon contribution to the heat capacity at room temperature is larger than the electronic contribution [37]. In this limit, the parameters G_{pp}/C_p and G_{cp}/C_p of the TTM are small compared to G_{cp}/C_c, and phonon-phonon coupling does not contribute significantly to the cooling rate. For this case the carrier temperature decays at a rate $k_+ \simeq G_{cp}/C_c = k_0$ with a negligible slow component ($A_- \simeq 0$). To elucidate the microscopic processes contributing to G_{cp} we discuss the following simple approach. We assume scattering from a single LO phonon mode cools electrons within a single, spherical band. The rate of change of the carrier temperature can be approximated by $dT_c/dt = -k_0(T_c - T_p)$. This expression is equivalent to the Fröhlich energy loss rate described previously [20], which allows the temperature loss rate to be linked to the strength of the electron-LO phonon interaction, mediated by the Fröhlich coupling constant, α. This approach yields

$$k_+ \simeq k_0 = \frac{G_{cp}}{C_c} \simeq \frac{4\alpha k_B}{3\sqrt{\pi}\hbar}\frac{\Theta^{\frac{5}{2}}K_0(\Theta/2T_c)}{\sqrt{T_c}(T_c-T_p)}\frac{\sinh\left[(T_c-T_p)\Theta/2T_cT_p\right]}{\sinh\left(\Theta/2T_c\right)}, \quad (8)$$

where $\Theta = \hbar\omega_{\mathrm{LO}}/k_B$ for an LO phonon with angular frequency ω_{LO}; K_0 is the modified Bessel function of the second kind; and the strength of the electron-LO phonon interaction is given by $\alpha = \frac{e^2}{4\pi\varepsilon_0\hbar}(\frac{m^*}{2\hbar\omega_{\mathrm{LO}}})^{1/2}(\frac{1}{\varepsilon_\infty}-\frac{1}{\varepsilon_s})$, where ε_s and ε_∞ are the static and high frequency dielectric constants and m^* is the bare electron mass. In the TTM model we assume that k_0 is a constant, rather than depending on the carrier temperature and the phonon temperature as described in Eq. (8). However, we can argue based on Eq. (8) that τ_+ decreases (k_+ increases) when the phonon frequency increases, or when the Fröhlich constant is higher.

Returning now to consider the general case including coupling between hot LO-phonons and the lattice ($k_+ \neq k_0$): the magnitude of G_{pp} is expected to be smaller than G_{cp} because the phonon-phonon interaction is an anharmonic process. There are different ways in which a zone-center LO phonon can decay: the Klemens channel, where an LO phonon decays into two acoustic phonons of opposite wave vectors [40]; the Ridley channel, creating a transverse optical and an acoustic phonon [41]; and the Vallée-Bogani channel, where another LO phonon and an acoustic phonon are produced [42]. Other channels such as the Barman-Srivastava and four-phonon processes are not relevant as they are connected, respectively, to the wurzite structure and to higher temperatures [43,44]. We therefore express the phonon-phonon coupling rate as

$$\frac{G_{pp}}{C_p} = \frac{1}{\tau_K} + \frac{1}{\tau_R} + \frac{1}{\tau_{VB}}, \quad (9)$$

where τ_K, τ_R, and τ_{VB} are the Klemens, Ridley, and Vallée-Bogani decay times. Explicit formulas for the various decay rates are reported in Barman and Srivastava [43].

The power of the TTM lies in the simple and quantitative picture of the various stages of cooling and in the connection to quantities that can be directly measured, concentrating all the microscopic parameters in few effective constants. Unfortunately, apart from a few reports for $MAPbI_3$ [45,46] accurate measurements of the heat capacity and of the coupling constants are lacking. Therefore, to estimate feasible values of the parameters, we first calculated how the decay time

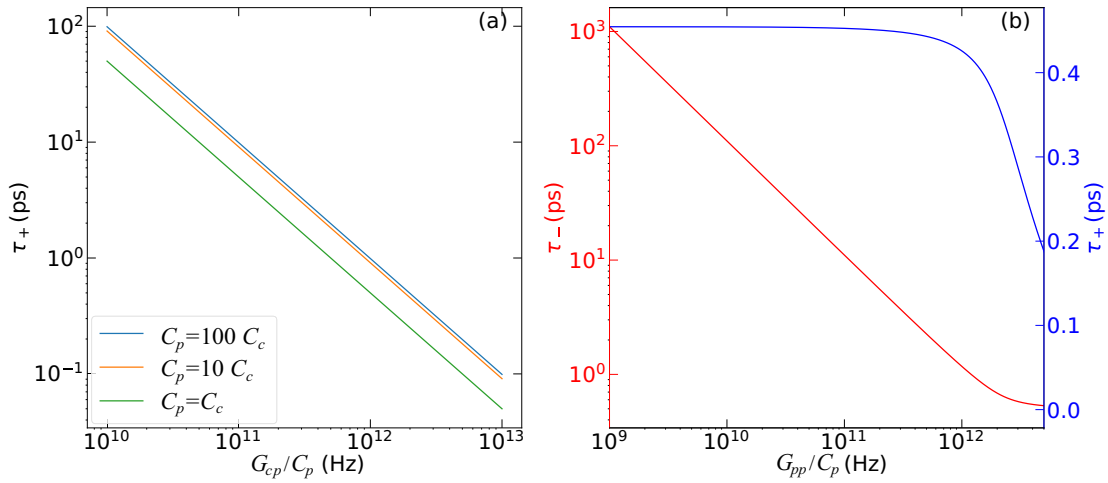

FIG. 4. (a) Calculated τ_+ from TTM as a function of G_{cp}/C_c, for different values of C_p/C_c. (b) Dependence of τ_+ (right, blue, linear y axis) and τ_- (left, red, logarithmic y axis) on G_{pp}/C_p, for a fixed $C_p = 10C_c$ and $G_{cp}/C_c = 2$ THz.

τ_+ varies with G_{cp}/C_c for realistic ratios of C_p and C_c (with $C_p > C_c$). The results are reported in Fig. 4(a) for $C_p/C_c = 1$, 10, and 100. The fast cooling time obtained by experiment is below 1 ps, which can be seen to require $k_0 = G_{cp}/C_c \sim 1$ THz.

A representative value of $k_0 = 2$ THz and $C_p/C_c = 10$ was adopted to explore how changing the phonon-phonon coupling strength G_{pp} alters τ_+ and τ_-, as reported in Fig. 4(b). The fast component was almost unchanged when the phonon-phonon coupling strength was varied over many orders of magnitude: τ_+ decreases substantially only for $G_{pp}/C_p \geqslant k_0 = 2$ THz. In stark contrast, the slow component τ_- was dramatically affected by G_{pp}: an order of magnitude reduction in coupling constant yields an order of magnitude increase in decay time. It is therefore possible to conclude that the initial fast decay in carrier temperature (τ_+) in stage (1) is dominated by the Fröhlich interaction, while the slower decay τ_- is linked to G_{pp}/C_p.

While the results from experiment (TAS) and phenomenological theory (TTM) presented thus far have given detailed information about hot carrier cooling in perovskites, obtaining $T_c(t)$ from TAS required detailed fits in a spectrally congested region (as discussed above). We therefore turned to optical pump terahertz probe spectroscopy to provide an independent experimental study of hot carrier cooling dynamics, and to determine the carrier mobility.

D. Optical-pump THz-probe spectroscopy

Wavelength-tunable optical pump terahertz probe spectroscopy was used to study hot carrier mobilities and cooling times at different excess energies. To allow a fair comparison of carrier cooling for different alloys, data were obtained at the same excess energies for different x.

1. Carrier cooling times from OPTP

In OPTP spectroscopy the photoconductivity $\Delta\sigma \propto -\Delta E/E$, where $\Delta E/E$ is the pump-induced relative change in the amplitude of the transmitted terahertz electric field. In the low frequency limit, the sheet photoconductance is $\Delta\sigma = en\mu$, where n is the sheet carrier density and μ is the sum of electron and hole mobilities. Hence $\Delta E/E$ is sensitive to the carrier mobility. When carriers are hot and high in the band their mobility will be lower, for instance, as a result of band nonparabolicity, leading to a small $\Delta E/E$. In contrast when carriers are cooler they have a higher mobility (larger $\Delta E/E$). The time for carriers to cool to the band edge can therefore be measured from the dynamical rise in $-\Delta E/E$ [20,24,25]. Given the reasonably large values of the Fröhlich coupling constant in metal halide perovskites the charge carriers are likely to form polarons.

Following this framework, the onset of photoconductivity was measured and is reported, for a few compositions and excess energies, in Fig. 5. No significant difference was observed in the onset dynamic for the perovskites for fluences between 10 and 300 μJcm^{-2}. The figure reports $-\Delta E/E$ for four samples: in Fig. 5(a) for a GaAs crystal, used as

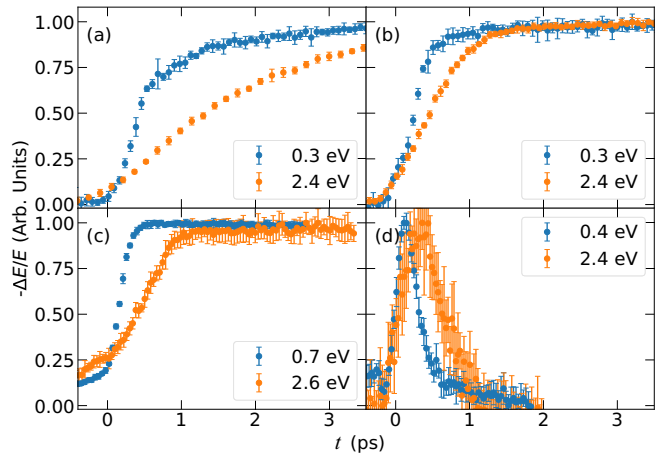

FIG. 5. Normalized photoinduced change in THz electric field for (a) GaAs and (b)–(d) $x = 1.0$, $x = 0.5$, and $x = 0.0$, respectively, at different excess energies above the band gap. The fluence was around 150 μJcm^{-2} for the perovskite samples and 5 μJcm^{-2} for the GaAs sample.

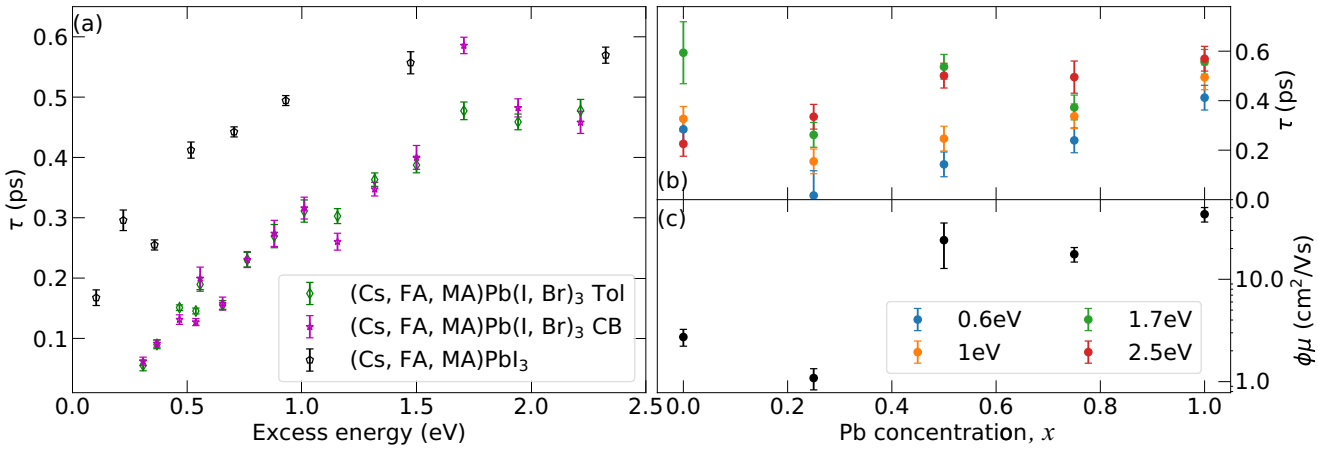

FIG. 6. (a) Carrier cooling times $\tau(E)$ measured from OPTP for three different samples: $y = 0$ and two samples with $y = 0.17$ made with two different solvents [27]. The two Br-added sample made with different solvents have a compatible carrier cooling time at each excess energy studied, which confirms the reproducibility of these experiments. Their values are, however, consistently smaller than the values obtained for the sample without Br. (b) Carrier cooling times $\tau(x, E)$ measured from OPTP for different compositions and excess energies. By increasing the excess energy for a specific sample the cooling times get longer. (c) Product of quantum yield and total carrier mobility, $\phi\mu$, for different compositions, and shown with a logarithmic y-axis to better illustrate the variation with x.

a reference, and for $Cs_{0.05}(FA_{0.83}MA_{0.17})_{0.95}Pb_xSn_{1-x}I_3$ with $x = 1.0$, $x = 0.5$ and $x = 0$ in Figs. 5(b), 5(c) and 5(d), respectively. In all four cases low and high excess energies are presented. As previously reported [20,24], the rise in GaAs is relatively quick, taking a few hundred fs to reach the maximum at low excess energy. At higher excess energy the rise becomes substantially slower due to intervalley scattering. For the perovskites the rise is faster than for GaAs, at all excess energies.

The $\frac{\Delta E}{E}$ dynamics were fitted by assuming the electrons are initially injected by the pump to a state with negligible mobility. Those carriers then pass (cool) to a lower state (equivalent to the band edge) with high mobility, before finally recombining. This approach yields

$$-\frac{\Delta E}{E} = A(e^{-t/\tau_R} - e^{-t/\tau}), \tag{10}$$

where τ is the rise time and τ_R is the recombination time. The full Sn sample had a fast (picosecond) recombination dynamic, likely caused by a high density of traps or a high background hole density [47], and consistent with its lower mobility (reported below) and a broader Urbach tail in the absorption. For Sn-rich perovskites, the relative ease of oxidizing Sn^{2+} to Sn^{4+} creates high defect densities, which can be mitigated against by defect control strategies [20,47–49] that were not adopted in this work. Equation (10) was therefore used to model data for $x = 0$ and $x = 0.25$. At larger x, τ_R increased to $\tau_R = 2.3$ ns for $x = 0.5$. In the case that $\tau_R \gg \tau$, Eq. (10) can be approximated to

$$-\frac{\Delta E}{E} = A(1 - e^{-t/\tau}). \tag{11}$$

This simplified version was applied to model data obtained for $x = 0.5$, 0.75, and 1.0, which had long recombination times exceeding 2 ns. The expression for $\Delta E/E$ was then convoluted with an instrument response function (IRF), assumed to be a Gaussian shape (standard deviation 150 fs), following the approach of Bretschneider *et al.* [21]. By including the IRF we can, in principle, recover times lower than the instrument response time (around 150 fs), and instead limited by the duration of the laser pulse (around 50 fs).

The carrier cooling times obtained from OPTP are reported in Fig. 6(a) for different excess energies for $x = 1$, $y = 0$ and for two samples (prepared with different anti-solvents) with $x = 1$, $y = 0.17$. Changing the antisolvent, used to promote crystal formation, from chlorobenzene (CB) to tolulene did not alter the cooling time τ for $x = 1$, although the solvent can modify the mobility of Sn-containing perovskites [27]. The measured times $\tau < 1$ ps are consistent with those previously measured for organic-inorganic lead perovskites by a variety of methods [8,21,50]. The influence of composition is discussed below in Sec. III E. At a given composition, τ increases with excess energy, for instance from 0.2 to 0.6 ps for $x = 1$, $y = 0$. This trend can be qualitatively explained with reference to the simple approach adopted in Eq. (8) based on the Fröhlich interaction [20]. In this picture, the energy loss time can be estimated as the loss of one phonon (with energy $\hbar\omega_{LO}$) in one scattering event τ_{LO}, then averaged over the Maxwell-Boltzmann distribution [51]. For energies higher than the LO phonon energy the cooling time increases with excess energy because more events are required to lose the initial energy.

2. *Comparison between OPTP and TAS*

The cooling time measured by OPTP, τ, is in good quantitative agreement with the fast cooling time τ_+ obtained from TAS when compared at similar excess energies. For instance, for $x = 1$, $y = 0$ and an excess energy 1.7 eV, TAS determined $\tau_+ = 0.35 \pm 0.04$ ps, while OPTP determined $\tau = 0.39 \pm 0.04$ ps at a similar fluence. Changing the fluence did not alter the Fröhlich cooling time obtained from either technique.

Individually the two experimental methods employed have advantages and disadvantages. In the OPTP experiment, when

carriers have relaxed in energy to close to the band edge, the mobility will not differ significantly from the Γ point value. For this reason, OPTP does not provide information about τ_-, and just tracks τ_+. OPTP therefore provides a straightforward tool to measure the initial, rapid carrier cooling process (the Fröhlich stage), without the modeling assumptions of TAS. However, TAS probes the carrier's energy distribution close to the band gap, and hence has the advantage of being more sensitive to the cooling dynamics at lower carrier temperatures (later times) than OPTP. Together, they enable a complete picture of carrier cooling and mobility, as is now discussed.

E. Influence of composition on cooling dynamic

The hot carrier cooling dynamics were strongly influenced by the Pb/Sn ratio, although in different ways for the different cooling stages. Considering first the influence of composition on cooling stage (1), we examine results from OPTP at lower excess energy (0.6 and 1.0 eV), where carriers were directly injected closer to the band edge. As reported in Fig. 6(b), the cooling time is longest for the full lead sample ($\tau = 0.4$ ps), and steadily shortens with increasing Sn concentration (lower x) to a minimum at $x = 0.25$. In this case the fit was limited by the instrument response function, and we can only conclude that $\tau \leqslant 100$ fs. For the full tin sample the cooling time increased marginally to $\tau = 300$ fs.

These differences can be assigned to a modification of the carriers' effective mass or to changes in the LO phonon modes. Indeed, as Eq. (8) indicates, the decay rate $k_0 = G_{cp}/C_e$ in the Fröhlich regime is a function of ω_{LO} and m^*. The phonon modes for $x = 0$ will be higher in frequency in general than for $x = 1$ since Sn is lighter than Pb: this trend can be seen for instance in the Debye temperatures for $MASnI_3$ (230 K) and $MAPbI_3$ (175 K) [52]. A larger phonon frequency increases k_0, consistent with the lower τ and τ_+ observed in experiment for smaller x. Additionally, the prominent band bowing for the alloys implies changes to the effective mass, which will modify α and thereby k_0. This may account for the apparent minimum in τ at $x = 0.25$ rather than at $x = 0$. In particular it will be intriguing to establish whether the nonlinear behavior of the band gap of the alloy (evident in Fig. 1) is driven by crystallographic changes that also create bowing in the phonon frequencies.

For the pure Pb compound the partial substitution of I by Br induces a faster cooling time, as can be seen in Fig. 6(a). Br substitution is known to blue-shift the frequencies of the optical phonons associated with the metal halide octahedra [53]. The enhanced phonon frequency may increase the electron-phonon cooling rate, for the same reasons as outlined for Sn substitution.

Examining instead the high excess energy regime (e.g., 1.7 or 2.5 eV) the Fröhlich cooling time does not appear to vary substantially with x for the $x = 0.5$–1.0 samples, as can be seen in both OPTP (Fig. 6) and TAS (Fig. 3) results. At higher excess energies the approximations in Eq. (8) are not valid, and the cooling rate will depend on details of the electronic bandstructure (e.g., the influence of band nonparabolicity or different bands).

The HPB can be accessed at high excess energies and studied via TAS, and the influence of x on the slow component (τ_-) is reported in the inset to Fig. 3. All compositions show a HPB, with τ_- substantially larger than τ_+ for all samples studied. Remarkably, the slowest cooling dynamic occurs for the mixed lead-tin compound with $x = 0.5$: $\tau_- = 120$ ps is an order of magnitude larger than for $x = 0$ and $x = 1$. Note that the short recombination time of the full Sn-based perovskite ($\sim$1 ps) means that there may be a substantial error in the value $\tau_-(x = 0) = 8$ ps for that composition.

A study of hot carrier cooling in $FAPb_xSn_{1-x}I_3$ has been reported recently [19], with slow components as long as 500 ps claimed (although extrapolated outside the 100 ps experimental time window). Here, a quantitative understanding of slower hot carrier cooling (increased τ_-) in the HPB regime can be given using the TTM formalism described above. With reference to Fig. 4(b), an order of magnitude reduction in G_{pp}/C_p is required to account for the larger τ_- observed for the Pb-Sn alloy. One explanation is that the phonon-phonon interaction strength, G_{pp}, is suppressed in the mixed compound in comparison to the "pure" compounds, as a result of a reduction in the Klemens decay rate [see Eq. (9)] created by a larger phonon "band gap." The phonon band gap, defined as the difference in the maximum acoustic phonon energy and minimum optical phonon energy, is expected to increase when atoms with a significant mass difference are coupled [54], as for the mixed Pb-Sn alloys studied here. The relevant hot LO-phonons are at low frequencies (in the THz range), such as the bend and stretch modes of the metal halide octahedra [53]. As an alternative mechanism to account for the enhanced τ_-, changes in C_p may also contribute, in particular as Debye temperatures vary with composition.

F. Carrier mobility

The product $\phi\mu$ of the total mobility (μ, the sum of hole and electron mobility) and the yield of free charges (ϕ) was extracted from the measured THz photoconductivity using a standard method [23], and is reported in Fig. 6(c). For samples with $x \geqslant 0.5$ the mobility is relatively higher ($\phi\mu \gtrsim 20$ cm^2/Vs) in comparison to $x < 0.5$, where $\phi\mu \leqslant 2$ cm^2/Vs. $\phi\mu$ therefore varies more dramatically with composition than the cooling time τ, which can be seen in Fig. 6(b) to vary by a factor of 3. This can be understood as follows: τ is controlled by inelastic LO-phonon and acoustic phonon scattering processes, which are intrinsic to a given material. The mobility is linked to the total momentum scattering rate, however, which has additional contributions from extrinsic scattering process such as carrier-impurity scattering, alloy scattering and interface roughness scattering. Thus the large variation in $\phi\mu$ with x may be due to extrinsic factors such as variations in grain size, crystallinity, alloy disorder, and defect concentration. It is therefore more informative to use the carrier cooling τ to discuss changes in phonon scattering rates with composition than to look at $\phi\mu$.

Finally, by comparing the results of OPTP with the results of TAS we can conclude that the hot carriers in the hot phonon bottleneck regime have a mobility comparable to the cold carriers. For instance, the temperatures deduced from TAS allow one to identify that for $t > 1$ ps the perovskite was in the HPB regime, with $T \leqslant 700$ K. Under the same experimental conditions (same excitation fluence, excess energy, and time

delay), the photoconductivity reported by OPTP has already reached a plateau (Fig. 5), indicating that warm carriers in the hot-phonon bottleneck regime are as mobile as cold carriers.

IV. CONCLUSION

In this work the influence of composition upon hot carrier cooling rates and the carrier mobility of mixed lead-tin perovskites was explored, via a combination of optical pump terahertz probe spectroscopy, transient absorption spectroscopy, and quantitative modeling. This systematic analysis has further identified the similarities and differences in the quantities measured by the experimental techniques, thereby resolving the apparent contradiction in the literature of disparate cooling times reported by OPTP and TAS.

The cooling dynamic measured through transient absorption spectroscopy was successfully described by a three temperature model, which allowed us to quantitatively model data in the different cooling regimes. The fast initial Fröhlich cooling, linked to the electron-LO phonon coupling, varied with Sn content in a way consistent with a simple model of the cooling rate. Within the hot-phonon-bottleneck regime elevated carrier temperatures were maintained by the fast carrier-LO phonon interaction, but with a substantially slower phonon decay rate for the mixed compound.

The conclusion that carrier mobilities remain high during the hot phonon bottleneck regime has profound implications for the feasibility and implementation of hot-carrier solar cells based on perovskite semiconductors. The carrier diffusivity, D, will be higher in the hot carrier regime as a result of the increased T_c and because μ remains high. Taken together with the insights gained from the model introduced, these findings suggest possible new directions for the design and implementation of future perovskite devices with optimised carrier cooling profiles. For instance, for hot carrier solar cells elevated carrier temperatures over longer time periods are desirable, which can be achieved by designing perovskite materials to have lower LO-phonon decay rates, or higher phonon heat capacities.

ACKNOWLEDGMENTS

The authors acknowledge the Engineering and Physical Sciences Research Council (EPSRC) for financial support under Grant No. EP/N010825/1. K.D.G.I.J. acknowledges funding from the Equality Foundation of Hong Kong. The data that support the findings of this study are openly available at http://wrap.warwick.ac.uk/134788, reference number 134788.

[1] W. Zhang, G. E. Eperon, and H. J. Snaith, Metal halide perovskites for energy applications, Nat. Energy **1**, 16048 (2016).

[2] J. Huang, Y. Yuan, Y. Shao, and Y. Yan, Understanding the physical properties of hybrid perovskites for photovoltaic applications, Nat. Rev. Mater. **2**, 17042 (2017).

[3] N. Arora, M. I. Dar, A. Hinderhofer, N. Pellet, F. Schreiber, S. M. Zakeeruddin, and M. Grätzel, Perovskite solar cells with CuSCN hole extraction layers yield stabilized efficiencies greater than 20%, Science **358**, 768 (2017).

[4] F. Zhang and K. Zhu, Additive engineering for efficient and stable perovskite solar cells, Adv. Energy Mater. **10**, 1902579 (2020).

[5] B. R. Sutherland and E. H. Sargent, Perovskite photonic sources, Nat. Photon. **10**, 295 (2016).

[6] L. M. Herz, Charge-Carrier mobilities in metal halide perovskites: Fundamental mechanisms and limits, ACS Energy Lett. **2**, 1539 (2017).

[7] S. Kahmann and M. A. Loi, Hot carrier solar cells and the potential of perovskites for breaking the Shockley-Queisser limit, J. Mater. Chem. C **7**, 2471 (2019).

[8] Y. Yang, D. P. Ostrowski, R. M. France, K. Zhu, J. Van De Lagemaat, J. M. Luther, and M. C. Beard, Observation of a hot-phonon bottleneck in lead-iodide perovskites, Nat. Photon. **10**, 53 (2016).

[9] Z. Guo, Y. Wan, M. Yang, J. Snaider, K. Zhu, and L. Huang, Long-range hot-carrier transport in hybrid perovskites visualized by ultrafast microscopy, Science **356**, 59 (2017).

[10] M. B. Price, J. Butkus, T. C. Jellicoe, A. Sadhanala, A. Briane, J. E. Halpert, K. Broch, J. M. Hodgkiss, R. H. Friend, and F. Deschler, Hot-carrier cooling and photoinduced refractive index changes in organic-inorganic lead halide perovskites, Nat. Commun. **6**, 8420 (2015).

[11] P. P. Joshi, S. F. Maehrlein, and X. Zhu, Dynamic screening and slow cooling of hot carriers in lead halide perovskites, Adv. Mater. **31**, 1803054 (2019).

[12] H. H. Fang, S. Adjokatse, S. Shao, J. Even, and M. A. Loi, Long-lived hot-carrier light emission and large blue shift in formamidinium tin triiodide perovskites, Nat. Commun. **9**, 243 (2018).

[13] J. S. Manser and P. V. Kamat, Band filling with free charge carriers in organometal halide perovskites, Nat. Photonics **8**, 737 (2014).

[14] G. Xing, N. Mathews, S. S. Lim, Y. M. Lam, S. Mhaisalkar, and T. C. Sum, Long-Range balanced electron- and hole-transport lengths in organic-inorganic $CH_3NH_3PbI_3$, Science **342**, 344 (2013).

[15] S. D. Stranks, G. E. Eperon, G. Grancini, C. Menelaou, M. J. P. Alcocer, T. Leijtens, L. M. Herz, A. Petrozza, and H. J. Snaith, Electron-Hole diffusion lengths exceeding, Science **342**, 341 (2013).

[16] J. Fu, Q. Xu, G. Han, B. Wu, C. H. A. Huan, M. L. Leek, and T. C. Sum, Hot carrier cooling mechanisms in halide perovskites, Nat. Commun. **8**, 1300 (2017).

[17] G. J. Hedley, C. Quarti, J. Harwell, O. V. Prezhdo, D. Beljonne, and I. D. Samuel, Hot-Hole cooling controls the initial ultrafast relaxation in methylammonium lead iodide perovskite, Sci. Rep. **8**, 8115 (2018).

[18] J. Chen, M. E. Messing, K. Zheng, and T. Pullerits, Cation dependent hot carrier cooling in halide perovskite nanocrystals, J. Am. Chem. Soc. **141**, 3532 (2019).

[19] S. D. Verma, Q. Gu, A. Sadhanala, V. Venugopalan, and A. Rao, Slow carrier cooling in hybrid Pb' Sn halide perovskites, ACS Energy Lett. **4**, 736 (2019).

[20] M. Monti, S. X. Tao, M. Staniforth, A. Crocker, E. Griffin, A. Wijesekara, R. A. Hatton, and J. Lloyd-Hughes, Efficient intraband hot carrier relaxation in the perovskite semiconductor $Cs_{1-x}Rb_xSnI_3$ mediated by strong electron-phonon coupling, J. Phys. Chem. C **122**, 20669 (2018).

[21] S. A. Bretschneider, I. Ivanov, H. I. Wang, K. Miyata, X. Zhu, and M. Bonn, Quantifying polaron formation and charge carrier cooling in lead-iodide perovskites, Adv. Mater. **30**, 1 (2018).

[22] A. Burgos-Caminal, J. M. Moreno-Naranjo, A. R. Willauer, A. A. Paraecattil, A. Ajdarzadeh, and J.-E. Moser, Hot carrier mobility dynamics unravel competing sub-ps cooling processes in lead halide perovskites arXiv:1909.04589.

[23] R. L. Milot, G. E. Eperon, H. J. Snaith, M. B. Johnston, and L. M. Herz, Temperature-Dependent charge-carrier dynamics in $CH_3NH_3PbI_3$ perovskite thin films, Adv. Funct. Mater. **25**, 6218 (2015).

[24] M. C. Beard, G. M. Turner, and C. A. Schmuttenmaer, Transient photoconductivity in GaAs as measured by time-resolved terahertz spectroscopy, Phys. Rev. B **62**, 15764 (2000).

[25] J. Lloyd-Hughes, Generalized conductivity model for polar semiconductors at terahertz frequencies, Appl. Phys. Lett. **100**, 122103 (2012).

[26] A. Sridharan, N. K. Noel, H. Hwang, S. Hafezian, B. P. Rand, and S. Kéna-Cohen, Time-resolved imaging of carrier transport in halide perovskite thin films and evidence for nondiffusive transport, Phys. Rev. Mater. **3**, 125403 (2019).

[27] R. M. I. Bandara, K. D. G. I. Jayawardena, S. O. Adeyemo, S. J. Hinder, J. A. Smith, M. H. Thirimanne, N. C. Wong, F. M. Amin, B. G. Freestone, A. J. Parnell, D. G. Lidzey, H. J. Joyce, R. A. Sporea, and S. R. P. Silva, Tin(iv) dopant removal through anti-solvent engineering enabling tin based perovskite solar cells with high charge carrier mobilities, J. Mater. Chem. C **7**, 8389 (2019).

[28] S. Kahmann, S. Shao, and M. A. Loi, Cooling, scattering, and recombination-the role of the material quality for the physics of tin halide perovskites, Adv. Funct. Mater. **29**, 1902963 (2019).

[29] M. Saliba, T. Matsui, J. Y. Seo, K. Domanski, J. P. Correa-Baena, M. K. Nazeeruddin, S. M. Zakeeruddin, W. Tress, A. Abate, A. Hagfeldt, and M. Grätzel, Cesium-containing triple cation perovskite solar cells: Improved stability, reproducibility and high efficiency, Energy Environ. Sci. **9**, 1989 (2016).

[30] E. S. Parrott, T. Green, R. L. Milot, M. B. Johnston, H. J. Snaith, and L. M. Herz, Interplay of structural and optoelectronic properties in formamidinium mixed tin-lead triiodide perovskites, Adv. Funct. Mater. **28**, 1 (2018).

[31] J. A. Van Vechten and T. K. Bergstresser, Electronic structures of semiconductor alloys, Phys. Rev. B **1**, 3351 (1970).

[32] S. A. Bretschneider, F. Laquai, and M. Bonn, Trap-Free hot carrier relaxation in lead-halide perovskite films, J. Phys. Chem. C **121**, 11201 (2017).

[33] F. Deschler, M. Price, S. Pathak, L. E. Klintberg, D. D. Jarausch, R. Higler, S. Hüttner, T. Leijtens, S. D. Stranks, H. J. Snaith, M. Atatüre, R. T. Phillips, and R. H. Friend, High photoluminescence efficiency and optically pumped lasing in solution-processed mixed halide perovskite semiconductors, J. Phys. Chem. Lett. **5**, 1421 (2014).

[34] K. Miyata, D. Meggiolaro, M. Tuan Trinh, P. P. Joshi, E. Mosconi, S. C. Jones, F. De Angelis, and X. Y. Zhu, Large polarons in lead halide perovskites, Sci. Adv. **3**, e1701217 (2017).

[35] B. T. Diroll and R. D. Schaller, Intraband cooling in all-inorganic and hybrid organic-inorganic perovskite nanocrystals, Adv. Funct. Mater. **29**, 1901725 (2019).

[36] T. Hata, G. Giorgi, and K. Yamashita, The effects of the organic-inorganic interactions on the thermal transport properties of $CH_3NH_3PbI_3$, Nano Lett. **16**, 2749 (2016).

[37] R. H. M. Groeneveld, R. Sprik, and A. Lagendijk, Femtosecond spectroscopy of electron-electron and electron-phonon energy relaxation in Ag and Au, Phys. Rev. B **51**, 11433 (1995).

[38] R. D. Averitt and A. J. Taylor, Ultrafast optical and far-infrared quasiparticle, J. Phys. Condens. Matter **14**, R1357 (2002).

[39] A. G. Kontos, A. Kaltzoglou, E. Siranidi, D. Palles, G. K. Angeli, M. K. Arfanis, V. Psycharis, Y. S. Raptis, E. I. Kamitsos, P. N. Trikalitis, C. C. Stoumpos, M. G. Kanatzidis, and P. Falaras, Structural stability, vibrational properties, and photoluminescence in $CsSnI_3$ perovskite upon the addition of SnF_2, Inorg. Chem. **56**, 84 (2017).

[40] P. G. Klemens, Anharmonic decay of optical phonons, Phys. Rev. **148**, 845 (1966).

[41] B. K. Ridley, Electron scattering by confined LO polar phonons in a quantum well, Phys. Rev. B **39**, 5282 (1989).

[42] F. Vallée and F. Bogani, Coherent time-resolved investigation of LO-phonon dynamics in GaAs, Phys. Rev. B **43**, 12049 (1991).

[43] S. Barman and G. P. Srivastava, Long-wavelength nonequilibrium optical phonon dynamics in cubic and hexagonal semiconductors, Phys. Rev. B **69**, 235208 (2004).

[44] D. J. Ecsedy and P. G. Klemens, Thermal resistivity of dielectric crystals due to four-phonon processes and optical modes, Phys. Rev. B **15**, 5957 (1977).

[45] T. A. Tyson, W. Gao, Y. S. Chen, S. Ghose, and Y. Yan, Large thermal motion in Halide Perovskites, Sci. Rep. **7**, 9401 (2017).

[46] A. Glushkova, K. Mantulnikovs, G. Giriat, K. Semeniuk, L. Forró, E. Horváth, and A. Arakcheeva, Effect of thermal cycling on the structural evolution of methylammonium lead iodide monitored around the phase transition temperatures, Sol. RRL **3**, 1900044 (2019).

[47] R. L. Milot, M. T. Klug, C. L. Davies, Z. Wang, H. Kraus, H. J. Snaith, M. B. Johnston, and L. M. Herz, The effects of doping density and temperature on the optoelectronic properties of formamidinium tin triiodide thin films, Adv. Mater. **30**, 1804506 (2018).

[48] R. Lin, K. Xiao, Z. Qin, Q. Han, C. Zhang, M. Wei, M. I. Saidaminov, Y. Gao, J. Xu, M. Xiao, A. Li, J. Zhu, E. H. Sargent, and H. Tan, Monolithic all-perovskite tandem solar cells with 24.8 comproportionation to suppress Sn(ii) oxidation in precursor ink, Nature Energy **4**, 864 (2019).

[49] K. D. G. I. Jayawardena, R. M. I. Bandara, M. Monti, E. Butler-Caddle, T. Pichler, H. Shiozawa, Z. Wang, S. Jenatsch, S. J. Hinder, M. G. Masteghin, M. Patel, H. M. Thirimanne, W. Zhang, R. A. Sporea, J. Lloyd-Hughes, and S. R. P. Silva, Approaching the Shockley-Queisser limit for fill factors in lead-tin mixed perovskite photovoltaics, Journal of Materials Chemistry A **8**, 693 (2020).

[50] T. R. Hopper, A. Gorodetsky, J. M. Frost, C. Müller, R. Lovrincic, and A. A. Bakulin, Ultrafast intraband spectroscopy of hot-carrier cooling in lead-halide perovskites, ACS Energy Lett. **3**, 2199 (2018).

[51] K. Seeger, *Semiconductor Physics: An Introduction*, 9th ed., (Springer, Berlin, 2004), p. 208.

[52] J. Feng, Mechanical properties of hybrid organic-inorganic $CH_3NH_3BX_3$ (B = Sn, Pb; X = Br, I) perovskites for solar cell absorbers, APL Mater. **2**, 081801 (2014).

[53] Q. Sun, X. Liu, J. Cao, R. I. Stantchev, Y. Zhou, X. Chen, E. P. Parrott, J. Lloyd-Hughes, N. Zhao, and E. Pickwell-MacPherson, Highly sensitive terahertz thin-film total internal reflection spectroscopy reveals in situ photoinduced structural changes in methylammonium lead halide perovskites, J. Phys. Chem. C **122**, 17552 (2018).

[54] G. Conibeer, N. Ekins-Daukes, J. F. Guillemoles, D. Konig, E. C. Cho, C. W. Jiang, S. Shrestha, and M. Green, Progress on hot carrier cells, Sol. Energy Mater. Sol. Cells **93**, 713 (2009).